EUROFUSION WP15ER-PR(16) 15999

AH Nielsen et al.

Numerical simulations of blob dynamics with finite ion temperature

Preprint of Paper to be submitted for publication in
Plasma Physics and Controlled Fusion

This work has been carried out within the framework of the EUROfusion Consortium and has received funding from the Euratom research and training programme 2014-2018 under grant agreement No 633053. The views and opinions expressed herein do not necessarily reflect those of the European Commission.

Numerical simulations of blob dynamics with finite ion temperature

A. H. Nielsen[1], J. Juul Rasmussen[1], J. Madsen[1], G.S. Xu[2], V. Naulin[1], J.M.B. Olsen[1], M. Løiten[1], S. K. Hansen[1], N. Yan[2], L. Tophøj[1] and B.N. Wan[2]

[1] Department of Physics, Technical University of Denmark, Fysikvej, DK-2800 Kgs.-Lyngby, Denmark

[2] Institute of Plasma Physics, Chinese Academy of Sciences, Hefei 230031, People's Republic of China

E-mail: ahnie@fysik.dtu.dk

5 May 2016

Abstract. The transport of particles and energy into the scrape off layer (SOL) region at the outboard midplane of medium sized tokamaks, operating in low confinement mode, is investigated by applying the first principle HESEL model. HESEL is a four field drift-fluid model including finite electron and ion temperature effects, drift-wave dynamics on closed field lines, and sheath dynamics on open field lines. Particles and energy are mainly transported by intermittent blobs. Therefore, blobs have a significant influence on the corresponding profiles. The formation of a "shoulder" in the SOL density profile can be obtained by increasing the connection length, thus decreasing the efficiency of the SOL ability to remove plasma. As the ion pressure has a larger perpendicular but smaller parallel dissipation rate compared to the electron pressure, ion energy is transported far into the SOL. This implies that the ion temperature in the SOL exceeds the electron temperature with a factor 2-4 and will significantly broaden the power deposition profile.

1. Introduction

The success of particle and heat confinement in magnetically confined plasmas crucially depends on the control of transport in the outermost plasma region in contact with material surfaces. The transport regulates the particle and heat loads on the plasma-facing components, which must be controlled for a stable operation of high-power confinement devices such as ITER. An understanding of the physics governing transport at the boundary of magnetized plasmas is thus imperative.

In this paper we study the perpendicular particle and energy transport across the Last Closed Flux Surface (LCFS) using the 2-dimensional model, HESEL[1, 2, 3, 4]. HESEL is an energy conserving, four-field model based on the Braginskii equations[5]

governing the dynamics of a quasi-neutral, simple plasma. It describes interchange-driven, low-frequency turbulence in a plane perpendicular to the magnetic field at the outboard midplane. In the limit of constant ion pressure the model reduces to the ESEL model, which has successfully modeled fluctuations and profiles in JET[6], MAST[7], EAST[8] and TCV[9]. The HESEL model includes the transition from the confined region to the region of open field lines and the full development of the profiles across the LCFS. On closed field lines drift wave dynamics is included and on open field lines parallel losses from adiabatic expansion, electron heat conduction and sheath dissipation is included in the model. On both open and closed field lines we consider a single parallel length scale with length of the unstable parallel region.

Ion dynamics on the outboard midplane of a tokamak has both experimentally, [10, 11] and numerically [12, 1, 2] been shown to be a necessary, even essential, part in the L-H and L-I-H transitions. Furtheremore, ion dynamics is also important for the power deposition on the plasma facing components, such as the divertor. Experimentally there are only a few scrape-off-layer (SOL) diagnostics, which can measure electron temperature with a sampling rate necessary to analyze the dynamics of blobs, kHz − MHz, e.g. Langmuir probes and ball-pen-probes[13]. Measurements of ion temperature dynamics within the same sampling rate are unfortunately even more rare. The use of retarding field analyzers[14, 15] has shown that the ion temperature is typically $3-7$ times the electron temperature in the far SOL[14].

The efficiency of the SOL zto remove plasma can be estimated by the ratio of perpendicular to parallel particle transport, $\Gamma_\perp/\Gamma_\parallel$, if the perpendicular transport dominates, the midplane becomes disconnected from the divertor and a "shoulder" in the density profile forms in the far SOL. The transition from parallel dominated transport to perpendicular dominated transport can be estimated by an effective collisionality parameter[16]

$$\Lambda = \frac{L_c/c_s}{1/\nu_{ie}}\frac{\omega_i}{\omega_e}, \tag{1}$$

where L_c is the connection length from midplane to outer divertor leg, c_s is the sound speed, ν_{ie} the ion-electron collision frequency and ω_i and ω_e are the ion and electron gyro frequencies, respectively. For $\Lambda < 1$ it is assumed that the midplane will be connected to the sheath at the divertor, and for $\Lambda > 1$ the midplane will be disconnected, and hence the plasma can be transported far into the SOL, broadening the density profile. Experimentally, this transition has been observed at TCV[17] and more recently at ASDEX Upgrade (AUG), JET and COMPASS[18, 19]. Disconnection can be achieved by puffing a neutral gas into the divertor region or by recombination of plasma streaming into the divertor region. Deriving Eq. 1 the perpendicular transport of particles is assumed to depend on local plasma parameters. Coherent structures, blobs, are known to be responsible for this transport in the SOL on the outboard midplane. Their dynamics is not only determined by local plasma properties but also, and maybe even more important, by plasma conditions in the edge region, the region where they are created[20].

In this paper we will focus on blob dynamics to investigate their influence on particles and heat profiles. To characterise the structure of the blobs we will use the conditional average technique[21]. For the blobs contributions to the radial heat fluxes we will divide the fluxes into convective, conductive and triple parts, showing that all three parts contribute to the total flux. We will investigate in influence of the divertor sheath on the perpendicular transport and the relation to shoulder formation in the SOL region. To investigate the shoulder formation in the density profile we vary the parameter Λ, see Eq. 1, changing the connection length, L_c, but keeping all other input parameters as well, as divertor condition, constant.

The paper is organized as follows; in section 2 we present the HESEL model, in section 3 we present the result and finally in section 4 we present our conclusions.

2. Model equations

In this section we present the model equations applied in the present work, for a more detailed description of the model, see [4]. We base our description on the interchange instability of a non-uniformly magnetized plasma. In the case of an unstable equilibrium, the drive of the fluctuating motions is a convective transport of particles and heat outwards along the major radius of the toroidally magnetized plasma. A self-consistent description of this collective dynamics is here considered as a mechanism for intermittent turbulence in the plasma boundary region. In order to perform long simulations producing sufficient data to allow detailed statistical analysis, we reduce our description to two spatial dimensions and parallel dynamics along open magnetic-field lines in the SOL are parametrized. The model is solved in a local slab geometry, $(\hat{x}, \hat{y}, \hat{z})$, with the unit vector $\hat{\boldsymbol{z}}$ along the inhomogeneous toroidal magnetic field. The magnetic field is approximated by $B(r) = B_0(R + a)/(R + a + x)$, where R and a are the major and minor radius of the toroidal plasma and B_0 the magnetic field strength at the outboard midplane, respectively, see Fig. 1.

The model equations read[4]:

$$\frac{d}{dt}n + n\mathcal{K}(\phi) - \mathcal{K}(p_e) = \Lambda_n, \tag{2}$$

$$\frac{d^0}{dt}w^* + \{\nabla\phi, \nabla p_i\} - \mathcal{K}(p_e + p_i) = \Lambda_{w^*}, \tag{3}$$

$$\frac{3}{2}\frac{d}{dt}p_e + \frac{5}{2}p_e\mathcal{K}(\phi) - \frac{5}{2}\mathcal{K}\left(\frac{p_e^2}{n}\right) = \Lambda_{p_e}, \tag{4}$$

$$\frac{3}{2}\frac{d}{dt}p_i + \frac{5}{2}p_i\mathcal{K}(\phi) + \frac{5}{2}\mathcal{K}\left(\frac{p_i^2}{n}\right) - p_i\mathcal{K}(p_e + p_i) = \Lambda_{p_i}, \tag{5}$$

where n is particle density, $w^* = \nabla^2\phi + \nabla^2 p_i$ is the generalized vorticity, ϕ is the electrostatic potential, and p_e and p_i are electron and ion pressure, respectively. Temperatures are defined by $T_{i,e} = p_{i,e}/n$. The material derivative is defined as $\frac{d}{dt} = \frac{\partial}{\partial t} + \frac{1}{B(x)}\hat{\boldsymbol{z}} \times \nabla\phi \cdot \nabla$, except in the vorticity equation, Eq.3, where the magnetic field is taken as constant, B_0. The curvature operator is given as $\mathcal{K} = \nabla(\frac{1}{B(x)}) \cdot \hat{\boldsymbol{z}} \times \nabla$.

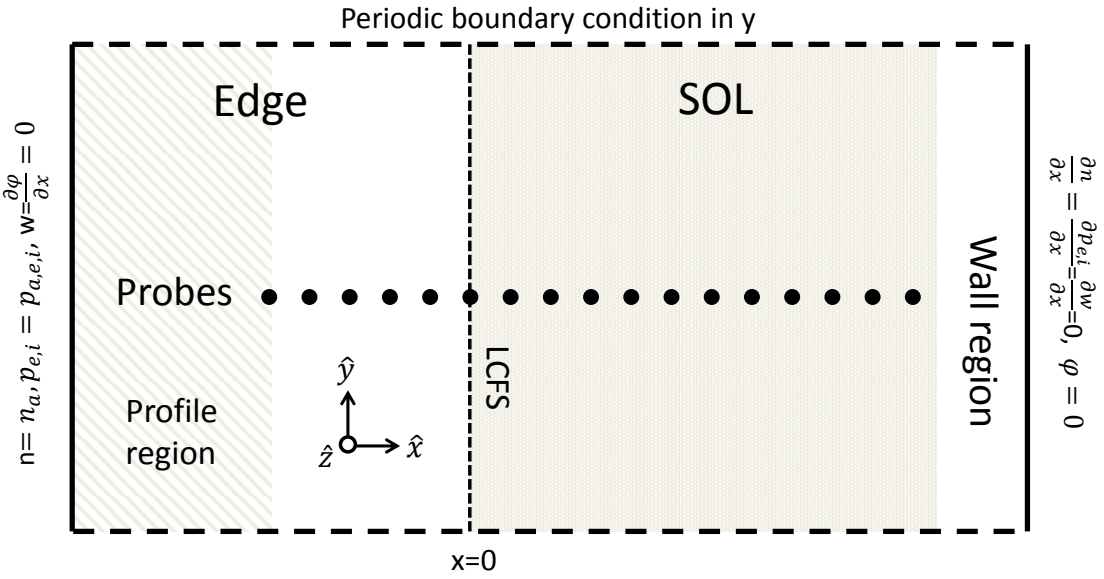

Figure 1: Setup of the simulation domain showing the closed field line region, the edge region including the inner part where prescribed profiles are dominant and the open field line region, SOL, where the parallel loss terms are active. Data time series of all fields are recorded by the numerical probes radially separated across the edge and SOL regions.

The generalized vorticity is the manifestation of the polarization current in the model and describes charge separation due to the inertia in the ion response to changes in the $\boldsymbol{E} \times \boldsymbol{B}$ and diamagnetic drifts.

At this point we introduce the so-called Bohm normalization defined by

$$\omega_{i0} t \to t, \ \frac{x}{\rho_s} \to x, \ \frac{T_{e,i}}{T_{e0}} \to T_{e,i}, \ \frac{e\phi}{T_{e0}} \to \phi, \ \frac{n}{n_0} \to n, \tag{6}$$

where $\omega_{i0} = eB_0/m_i$ the ion gyro frequency at magnetic-field strength at the outboard midplane, B_0, $\rho_s = \sqrt{T_{e0}/(m_i \omega_{i0}^2)}$ the cold-ion hybrid thermal gyro-radius and n_0 and T_{e0} are characteristic values of the particle density and electron temperature, respectively.

The right hand sides of Eqs. 2-5 represent perpendicular resistivity, perpendicular electron and ion heat conduction, ion viscosity, and parametrized parallel dynamics[4]:

$$\Lambda_n = D_e \nabla_\perp^2 n - \frac{n}{\tau} - \alpha \left(\tilde{T}_e + \frac{\bar{T}_e}{\bar{n}} \tilde{n} - \tilde{\phi} \right) - \frac{n - n_p}{\tau_p}, \tag{7}$$

$$\Lambda_{w^*} = D_i \nabla_\perp^2 w^* - \frac{w^*}{\tau} - \frac{\rho_s}{L_c} \left[1 - \exp\left(\phi_m - \frac{\phi_s}{T_{e,s}} \right) \right] - \alpha \left(\tilde{T}_e + \frac{\bar{T}_e}{\bar{n}} \tilde{n} - \tilde{\phi} \right), \tag{8}$$

$$\Lambda_{p_e} = \frac{5}{2} D_e \nabla_\perp^2 p_e + \left(\frac{16}{6} - \frac{5}{2} \right) \nabla \cdot (n \nabla_\perp T_e) - \frac{2}{9} \frac{p_e}{\tau} - \frac{2}{9} \frac{p_e}{\tau^{SH}}$$
$$- \alpha \bar{T}_e \left(\tilde{T}_e + \frac{\bar{T}_e}{\bar{n}} \tilde{n} - \tilde{\phi} \right) - \Theta - \frac{p_e - p_{e,p}}{\tau_p}, \tag{9}$$

$$\Lambda_{p_i} = D_i \nabla_\perp^2 p_i - D_i T_i \nabla_\perp^2 n - \frac{2}{9}\frac{p_i}{\tau} + \Theta - \frac{p_i - p_{i,p}}{\tau_p} + p_i \Lambda_{w^*}, \tag{10}$$

where the normalized neoclassic transport coefficients are given by

$$D_i = \left(1 + \frac{R}{a} q^2\right) \frac{\rho_{i0}^2 \nu_{ii}}{\rho_{s0}^2 \omega_{i0}},\ D_e = (1 + \frac{T_{i0}}{T_{e0}}) \left(1 + \frac{R}{a} q^2\right) \frac{\rho_{e0}^2 \nu_{ei}}{\rho_{s0}^2 \omega_{i0}}, \tag{11}$$

as derived in [4] and [6]. q is the safety factor and is in this model taken to be q_{95}. ρ_{e0} and ρ_{i0} are the electron and ion gyro radii. The term $\Theta = \frac{3m_e}{m_i}\nu_{ei}(p_e - p_i)$ in Eqs. 9-10 is the energy transfer between the electron and ion channels. We defined the mean and fluctuating components as;

$$\bar{f} = \frac{1}{L_y} \int_0^{L_y} f dy\ ,\ \tilde{f} = f - \bar{f}. \tag{12}$$

The terms involving parametrization of the parallel dynamics will be defined in the following subsection.

At the inner part of the edge region the density and pressure profiles are forced towards prescribed profiles, $n_p, p_{e,p}$ and $p_{i,p}$ with a time scale of τ_p, see Fig. 1. These profiles resemble typical profiles in the edge region of toroidally magnetized plasmas and act as sources of particles and heat, but also remove 'unphysical' instabilities otherwise generated in the vicinity of the inner boundary of the numerical system, a boundary which is of course not present in a tokamak.

For the density, pressures, generalized vorticity and generalized potential, $\phi^* = \phi + p_i$, we have used Dirichlet boundary conditions at the inner radial boundary and zero Neumann boundary conditions at the outer radial boundary. The Dirichlet conditions are in agreement with the prescribed profiles. All fields are periodic polodally. The set of equations are solved by employing a finite difference scheme with a symmetric, energy and enstrophy conserving discretisation of the nonlinear advection terms and an explicit third-order stiffly stable time integrator with diffusive terms treated implicitly using operator splitting[22].

2.1. Parametrization of the parallel dynamics

The ballooning characters of the radial transport in the edge region implies that the corresponding SOL region plasma source is concentrated to a region which extends 30 degrees above and below the outboard midplane[23]. In that respect we define a parallel ballooning length corresponding to the poloidal angle of this unstable region as: $L_b = qR$, see also [24, 25]. Using characteristic parameters from medium sized tokamaks like EAST and AUG we obtain $L_b \sim 8m$ and this length should be compared to the connection length from outboard midplane to outer divertor leg along the magnetic field lines, $L_c \sim 15\,\mathrm{m}$. As the plasma propagates radially outward it will expand along the magnetic field lines with a speed of $2M_\parallel c_s \sim 50,000\,\mathrm{m/s}$ where the hot ion sound speed, $c_s = \sqrt{(T_e + T_i)/m_i}$ has been calculated using $T_i = T_e = 25\,\mathrm{eV}$ and we have set the parallel Mach number to $M_\parallel = 0.5$. As the radial velocity of a blob typically will be a few percent of sound speed, $v_b/c_s \sim 0.01$, and for a width of the SOL of

$L_{SOL} \sim 0.05\,\mathrm{m} \sim 0.003 L_c$, we can safely assume that during the transit of a blob the plasma inside the flux tube will not have time reaching the divertor. As the blob expands parallel we will thus observe a decrease of the particle density, electron and ion pressures and the generalized vorticity.

Losses due to advection and electron heat conduction along the magnetic field lines in the SOL region are represented by the damping rates,

$$\frac{1}{\tau} = \frac{2M_{\parallel} c_s}{L_b},\ \frac{1}{\tau^{SH}} = \frac{X^{SH}_{\parallel,e}}{L_b^2}, \tag{13}$$

where the Spitzer-Härm (SH) expression for the electron heat diffusivity is given by $X^{SH}_{\parallel,e} = 3.16 V_e^2 \nu_{ee}$. Both the hot ion sound speed, c_s, and the electron thermal speed, V_e, are evaluated using the local value of electron and ion temperatures.

The compression of the parallel current is approximated on open field lines by a sheath dissipation term entering the vorticity in Eq. 8 where $\phi_m = \ln(\sqrt{m_i/2\pi m_e})$ is the Bohm potential. Using the poloidal average as a approximation for the flux surface average the connected divertor condition is modelled by using the full fields, i.e. $\phi_s = \bar{\phi} + \tilde{\phi}$ and $T_{e,s} = \bar{T}_e + \tilde{T}_e$ and the shielded or disconnected divertor condition is modelled by using only the mean fields, i.e. $\phi_s = \bar{\phi}$ and $T_{e,s} = \bar{T}_e$.

On closed field lines the compression of the parallel current is approximated by drift wave terms, i.e. the terms in Eqs. 7-9 involving α. The coefficient is given by, see also [24],

$$\alpha = \frac{2T_{e0}}{\nu_{ei} m_e L_{\parallel}^2 \omega_{i0}}, \tag{14}$$

where the parallel length scale is, unless otherwise stated, chosen as the parallel ballooning length, $L_{\parallel} = L_b = qR$. In deriving Eq. 14, we have assumed that the mean components of density, potential and electron temperature does not have any parallel variation, $\nabla_{\parallel}\bar{n} \sim \nabla_{\parallel}\bar{T}_n \sim \nabla_{\parallel}\bar{\phi} \sim 0$, and that second order terms can be neglected, $\tilde{n}\tilde{T}_e \sim 0$. We note that this representation is a significant simplification of the parallel dynamics on closed field lines and that it is quite sensitive to the choice of parallel length and reference electron temperature.

3. Numerical results

Typical parameters for HESEL simulations are parameters relevant for a medium size tokamak, such as EAST and ASDEX. Unless otherwise stated, the reference parameters used in this paper are; density $n_0 = 1.5 \times 10^{19}\,\mathrm{m}^{-3}$, electron temperature, $T_{e0} = 25\,\mathrm{eV}$, ion temperature, $T_{i0} = 25\,\mathrm{eV}$, magnetic field strength $B_0 = 1.9\,\mathrm{T}$, $q = q_{95} = 5.32$, major radius, $R = 1.65\,\mathrm{m}$, minor radius, $a = 0.5\,\mathrm{m}$, parallel connection length to divertor, $L_c = 15.0\,\mathrm{m}$. Subscript 0 refers to expected value in the vicinity of LCFS. With these parameters we obtain the following values for the Bohm normalized transport coefficients: $D_e = 0.0043$, $D_i = 0.073$, $1/\tau_0 = 0.000016$, $1/\tau_0^{SH} = 0.00098$ (the subscripts 0 refer to the damping rates calculated using the electron reference temperature, T_{e0})

and $\alpha = 0.000274$. The effective collisionality parameter are for these parameters given by Eq. 1: $\Lambda = 0.758$.

For the numerical domain, see Fig. 1, we have used $L_x = L_y = 250\,\rho_{\rm s}$ with an edge area of $L_{edge} = 90\,\rho_{\rm s}$, a SOL of $L_{SOL} = 125\,\rho_{\rm s}0$ and a wall shadow region of $L_{Wall} = 35\,\rho_{\rm s}$ where $\rho_s = 0.38\,$mm. In the wall shadow region the parallel connection length is reduced to 2.5 m and this region thus acts as a damping layer which also prevent reflections from the outer wall. The resolution was chosen to $N_x = N_y = 1024$.

3.1. Blob evolution

In Fig. 2 we show a snapshot of all the relevant fields from a HESEL simulation using the above parameters and for connected divertor condition. We observed two large coherent structures, blobs, with a radial diameter of $\sim 2\,$cm in the middle of the SOL. The blobs are clearly visible in all the fields. As connected divertor condition drains the kinetic energy of the blobs they quickly loses momentum, leaving them stationary in this part of the SOL, slowly being drained by parallel loses.

Figure 3 show the time evolution of signals from one of the numerical probes positioned in the SOL just outside the LCFS. The position is indicated by black dots on the density, temperatures and potential plots in Fig. 2. The intermittent nature of the system is clearly seen in all the plots. For the turbulent flux signals, $\Gamma_n = nv_x, \Gamma_{P_e} = nT_e v_x, \Gamma_{P_i} = nT_i v_x$, all the radial transport take place in $3-4$ localized events. We also observe that the ion temperature and heat flux are significantly larger than the electron temperature and heat flux. The electric potential variation follows density and temperature variations closely.

3.2. Conditional Average technique

The basic idea of a conditional analysis is discussed by, e.g. Johnsen et al.[21]. Two time records, A and B, of correlated, randomly varying signals are considered. One, say A, is used as a reference. For A we determined its maximum value, $A(t_*)$. If this value fulfils the prescribed condition, $(A(t_*) - \bar{A}) > \beta\sigma_A$ with $\bar{A}$ and σ_A being the mean and the RMS of A, a sub-series is then selected from signal B in the time interval $\{t_* - \tau; t_* + \tau\}$. Signal A is then zero-padded in a time interval $\{t_* - 2\tau; t_* + 2\tau\}$ and the procedure is repeated as long as the condition on A is fulfilled. The time τ is usually taken to be of the order of the correlation time for the signals. The selected time sequences will therefore always be non-overlapping. The resulting sets of sub-series are considered as independent conditional realizations for the ensuing statistical analysis. This technique is widely used in analyzing experimentally obtained data from e.g. Langmuir probes[26, 27, 28].

In Fig. 4 we show the results of the conditional averaging analysis applied to the time signals from numerical probes positioned radially in the SOL region and using the density signal as reference signal, A. Using the density signal also as signal B we observe a well-defined blob, which decreases in amplitude as it propagates across

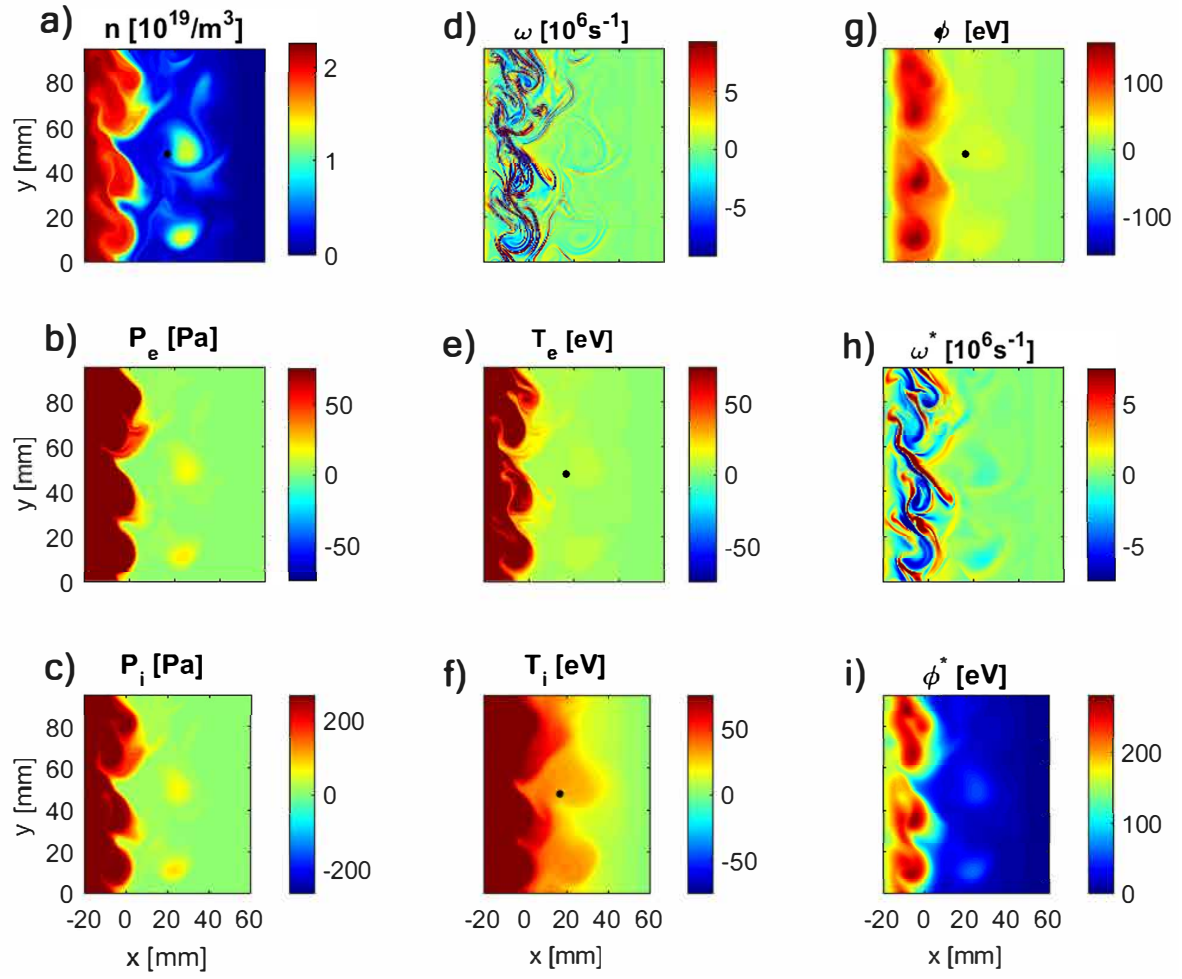

Figure 2: Snapshot of a HESEL simulation using connected divertor condition and for $t = 0.791\,\mathrm{ms}$. a) density, n, b) electron pressure, p_e, c) ion pressure, p_i, d) vorticity, w, e) electron temperatures, T_e, f) ion temperature, T_i, g) fluctuation electric potential, $\tilde{\phi}$, h) generalized vorticity, w^* and i) generalized potential, ϕ^*. The black dot in subplot a), e) and f) denotes the position of the probe in Fig. 3(a).

the SOL. As the blob reaches the middle of the SOL a significant broadening of the conditional signal is observed, consistent with the fact that the radial velocity of the blob significantly decreases around this radial position. The blob will therefore slowly decay and in this process it will expand due to perpendicular dissipation. Using one of the two temperatures as signal B we observed that the amplitudes and widths of the conditional average signals decreases significantly. As the electron heat conduction is much faster than the parallel advection, $1/\tau << 1/\tau^{SH}$, the electron temperature has nearly returned to the background level when the blob reaches the middle of the SOL, with a perturbation of $\Delta T_e \sim 5\,\mathrm{eV}$. The ion temperature perturbation, on the other hand, is still large, $\Delta T_i \sim 20\,\mathrm{eV}$. We also observe that the ion temperature profile is broader the the electron temperature profile, consistent with $D_e \ll D_i$.

Applying the conditional averaging technique to the electrical potential signal

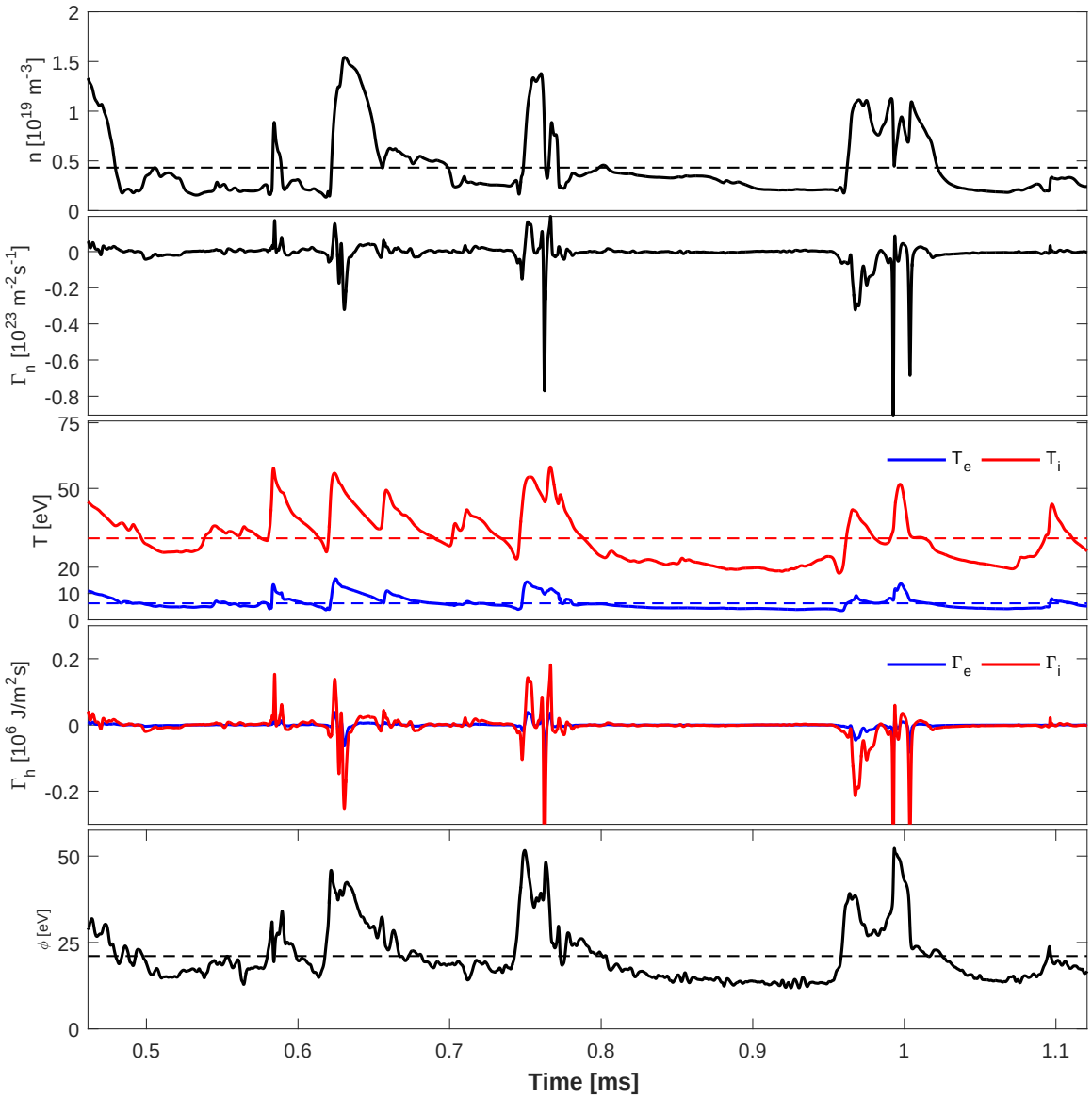

Figure 3: Time evolution of the density, the particle flux, the temperatures, the heat fluxes and the electric potential at a radial position $x = 18.0\,\mathrm{mm}$, see Fig. 2. Red curves correspond to ion dynamics while blue to the electrons.

reveals a signal somewhat similar to the electron temperature signal. Even though the potential is coupled to the electron temperature by the sheath term in the vorticity equations we observe that $\langle\phi\rangle > \phi_m \langle T_e\rangle$. Another notable feature of the potential signal is that the two polarities of the potential associated with a dipole are not observed here.

In Fig. 5(a) we show the radial temperature profiles of the maximum of the conditional averaged blob in Fig. 4(b) and (d). The ion temperature is 2 times larger than the electron temperature as the blob enters the SOL. This ratio increases to 3.5 for $x > 15\,\mathrm{mm}$, where it stays roughly constant. This results is consistent with experimental measurements using retarding field analyzers[14]. We note that this simulation uses the

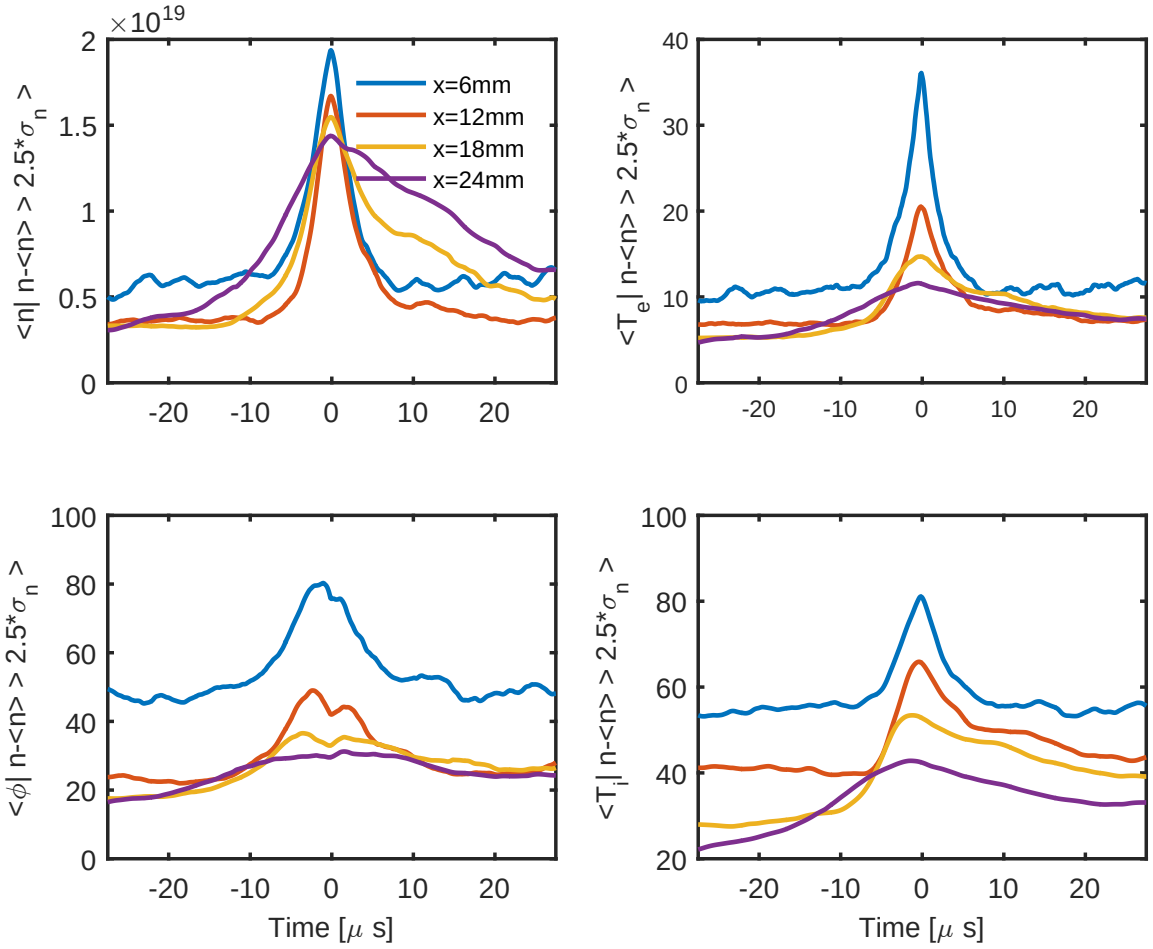

Figure 4: Conditional average wave forms of density, temperatures and electric potential using the density as the reference signal. Data takes from the HESEL simulation presented in Fig. 2.

same reference temperatures, $T_{e0} = T_{i0}$ as well as forced pressure profiles, $p_{e,p} = p_{i,p}$, in the inner edge region. In Fig. 5(b) we plot the radial profile of the number of events measured by the conditional average method from Fig. 4. Using the condition $n - \bar{n} > 2.5\sigma_n$ results in very few events inside LCFS, but just outside LCFS we observe a large number of events, ~ 170, which $1 - 2\,\mathrm{cm}$ into the SOL drops significantly to $\sim 20 - 50$ events across the last part of SOL region. Based on the amplitude of 90 eV of the ion temperature wave form closest to the LCFS we estimate that the blobs are created approximately 1 cm inside the LCFS.

3.3. Drift wave dynamics

In the previous papers, where the HESEL model was used to investigate the L–I–H transition[1, 2], the model only included the Interchange Mode (IM) modified by finite ion temperature effects and dissipation terms. This paper accounts for the influence of finite parallel wavelength and includes the Resistive Ballooning Mode (RBM)[29]. The

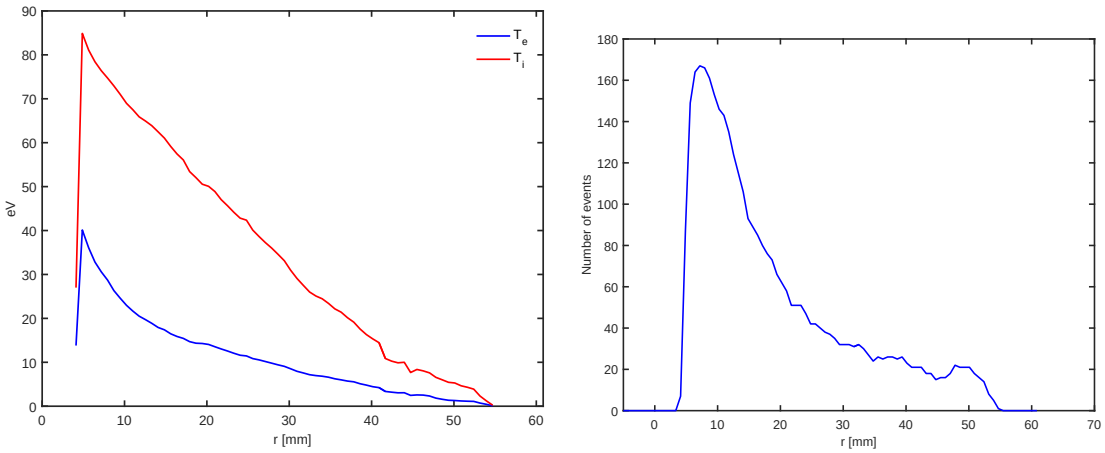

Figure 5: a) radial temperature profiles of the maximum value of the conditional averaged blob and b) the corresponding radial profile of number of events. Data derived from Fig. 4.

maximum linear growth rate in the IM peaks at a very low poloidal wave number and an instability with a wavelength of the width of the numerical box would typically be generated. For the RBM the linear growth rate increases from 0 with increasing k_θ to some maximum and a larger poloidal wave number will be expected to dominate.

In Fig. 6(a-c) we show three snapshots of the density at the time where the perturbation of the unstable plasma becomes visible. The simulations correspond to three different choices of the parallel length, $L_\parallel$, and thus different drift wave coefficients, α. As $L_\parallel$ decreases, i.e. increasing α, we observe a higher wave number in the density fluctuations. In Fig. 6(d-f) we show the corresponding time evolution of the 10 lowest poloidal wave numbers for the three cases. We observed mode number 3, 6 and 9 have the largest linear growth rate in the 3 simulations. This mode is also the mode observed in the turbulent initial phase, top row, and also connected to the characteristic size of the blobs observed in the SOL. If $L_\parallel$ is decreased to $qR/4$ or even shorter the plasma gradients will, for these set of plasma parameters, remain stable.

To gain a closer insight into the influence of the drift wave term we have derived the cross power spectral density for fluctuations. For two temporal signals, $h(t)$ and $g(t)$ obtained from the same numerical probe, see Fig. 1, the cross power spectral density is derived by Fourier transforming the cross-correlation function, $R_{h,g}(\tau) = \langle h(t)g(t+\tau)\rangle$. The complex cross power spectrum may be written as[28]

$$S(f) = |S(f)|\exp\left(i\theta(f)\right). \tag{15}$$

The quantities $|S|$ and θ are referred to as the amplitude and the cross phase-spectrum, respectively. The term $\theta(f)$ is directly giving the phase difference between h and g at the given frequency f. For the turbulent particle flux, $\Gamma(x,t) = h(x,t)g(x,t) = n(x,t)v_x(x,t)$ we plot in Fig. 7 $|S|$ and θ for two different radial positions; $x_1 = -4\,\mathrm{mm}$ and $x_2 = +8\,\mathrm{mm}$. For both positions we observe a relatively broad spectrum up to approximately 70 kHz, consistent with blobs of diameters of $\delta \sim 1-2\,\mathrm{cm}$ and with

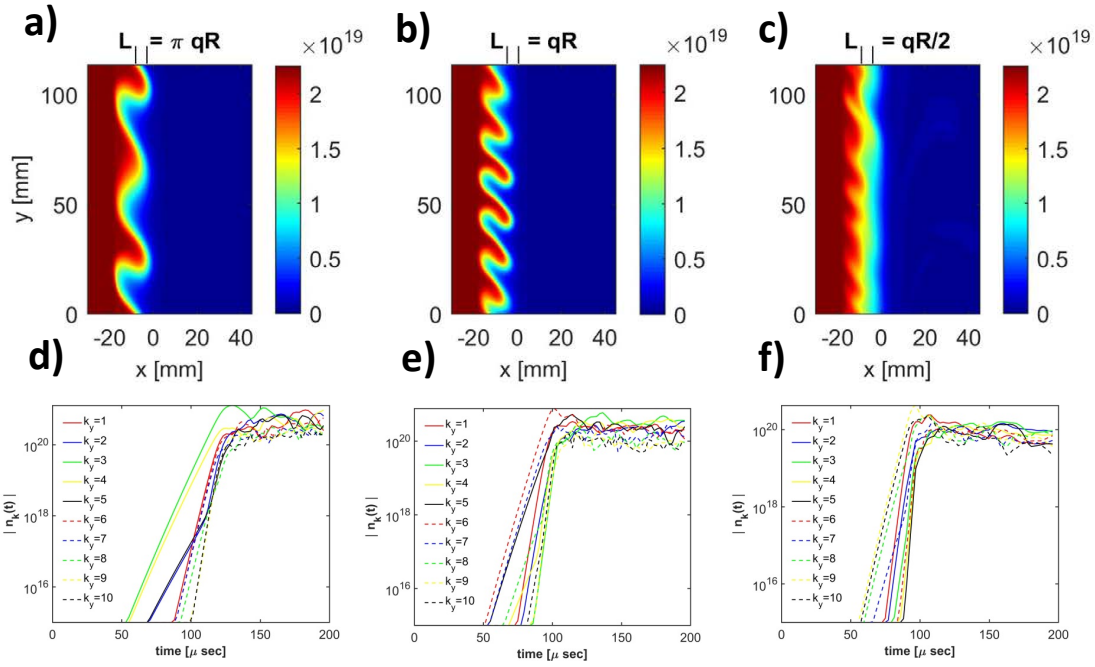

Figure 6: Individual simulations for three values of the parallel length, $L_{\|}$. a)-c) show snapshots of the density at the time where the perturbation of the unstable plasma become visible. d)-f) show the time evolution of the 10 lowest poloidal modes during the linear growth and turbulent saturation phases. Input parameters otherwise as for Fig. 2.

velocities of $v_b \sim 500 - 1.000\,\mathrm{m/s}$. The phase, θ, shows large fluctuations, but we generally observe negative phases inside the LCFS and likewise positive phases outside the LCFS, as also seen on Fig. 7. We notice that even with the change of sign the calculated phases are nearly all within $\pm\pi/2$, which correspond to a positive radial particle transport. Maximum transport is obtained for $\theta = 0$.

In Fig. 8 we display the radial profiles of $\langle\theta\rangle$ for a combination of density, electron and ion temperatures signals versus the radial velocity signal. $\langle\theta\rangle$ is calculated as a weighted average over all frequencies: $\langle\theta\rangle = \sum_k \theta_k S_k/Z$, where $Z = \sum_k S_k$. In the edge region, where the drift wave term is active, we observed a negative weighted phase difference for all three curves, whereas in the near SOL, $0 < x < 20\,\mathrm{mm}$, we observe a moderate positive weighted phase. In the far SOL, $x > 25\,\mathrm{mm}$, the weighted phase becomes approximately $\pi/2$, and turbulent transport will be significant reduced. This is in agreement with Fig. 5(b) as most blobs does not propagate into the far SOL. We note that we are not obtaining a phase difference near $\pm\pi/2$ as expected numerically for pure drift wave turbulence in the edge region, well inside the LCFS. This observation is somewhat in agreement with [30], where the presence of both drift wave and interchange dynamics make it impossible to separate the two effects.

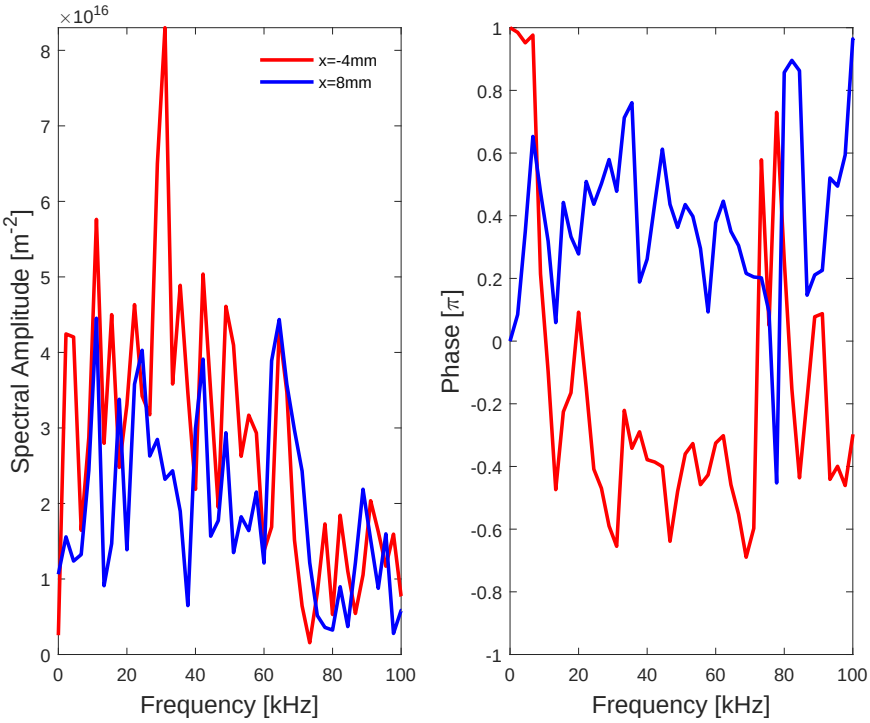

Figure 7: The amplitude, $S(f)$, and phase, $\theta(f)$, of the radial particle flux for two radial positions obtained from the cross power spectral density, see Eq. 15. Data takes from the HESEL simulation presented in Fig. 2.

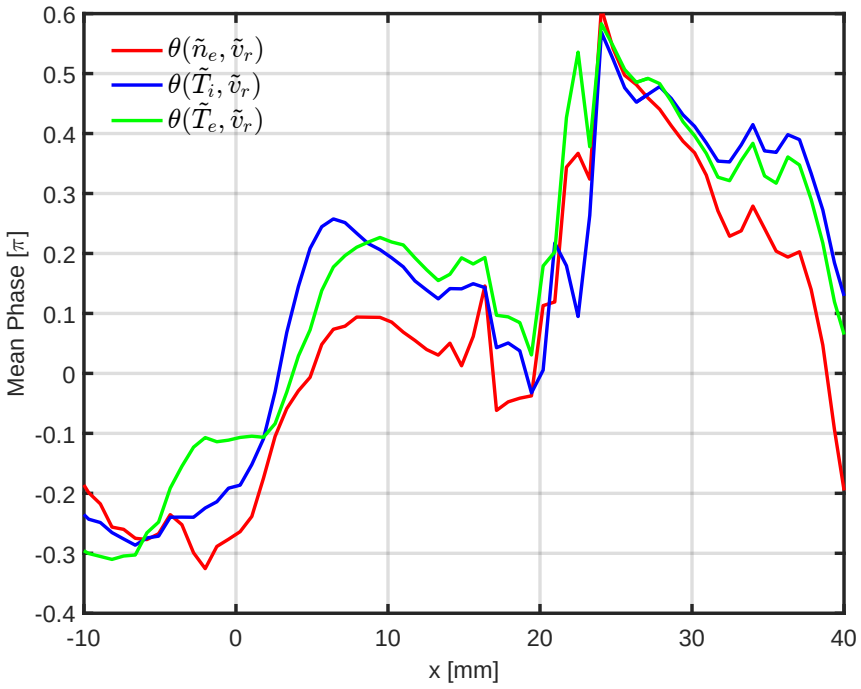

Figure 8: Radial profiles of the average phase difference calculated from the cross power spectral density. Data takes from the HESEL simulation presented in Fig. 2.

3.4. Radial profiles

In Fig. 9 we display the profiles of the density, temperatures, pressures, turbulent heat fluxes, and poloidal velocity. All the profiles have been averaged polodally and in time. The profiles all have sharp gradients close to the LCFS with density and electron temperature approaching a low value already 1 cm outside the LCFS, whereas the ion temperature profiles is much broader with a SOL width of ~ 4 cm. We decompose the turbulent ion and electron energy fluxes, $\langle n_e T_\alpha \tilde{v}_r \rangle$, $\alpha = \{i, e\}$, into a conductive heat flux, $\langle n_e \rangle \left\langle \tilde{T}_\alpha \tilde{v}_r \right\rangle$, a convective heat flux, $\langle T_\alpha \rangle \langle \tilde{n} \tilde{v}_r \rangle$, and to a pure non-linear flux, the so-called triple product, $\left\langle \tilde{n}_e \tilde{T}_\alpha \tilde{v}_r \right\rangle$. In the edge region the energy fluxes are dominated by the conductive part but in the SOL the largest contributions comes from the triple products, a consequence of the very intermittent dynamics in the SOL. The poloidal velocity shows a strong shear of $\sim 500.000\,\mathrm{s}^{-1}$ across the LCFS with a minimum just 5 mm outside the LCFS. We note that this position is the same as where the weighted phase changes sign, see Fig. 8.

We have performed a series of simulations in order to observe how our model behaves as the connection length, L_c, and thus the ratio of perpendicular to parallel transport, is changed, as mentioned in the introduction. In Fig. 10 we show the radial profiles of the normalised density and turbulent particle fluxes, $\Gamma_\perp$, for the cases $L_c = 5, 20, 40$ m corresponding to $\Lambda = 0.385, 1.54, 3.08$ and for both connected and disconnected divertor conditions. These simulations have been performed with $T_{e0} = T_{i0} = 20$ eV and $L_{SOL} = 31$ mm. For the connected simulations only one gradient length scale are observed throughtout the SOL for $\Lambda = 0.385$. For $\Lambda = 1.54$ and $\Lambda = 3.08$ we observe a plateau region in the middle of the SOL, which may be characterise as a shoulder region, see [18, 19]. The perpendicular particle flux profile gets broader as Λ increases, which demonstrate that the effective area, or wetted area, of the divertor increases. For a disconnected divertor the generated blobs can cross the SOL completely and enter the wall region. The SOL is only a transit region and we observe nearly constant density profiles. The perpendicular particle flux at the entrance to the wall region is more than 50% of the LCFS values, displaying in this case the inefficiency of the SOL to remove the plasma.

4. Conclusions

We have examined blob propagation across the SOL due to interchange dynamics on the outboard midplane of a tokamak using the 2D HESEL model. We have shown that blobs has a high ion temperature but low electron temperature perturbation in agreement with experimental observations, [14, 13]. This is perhaps the first time that the experimentally observed differences between the temperatures in the SOL has been modelled. Energy losses to plasma facing components, such as the divertor, thus depends heavily that the ion temperature dynamics.

The parallel dynamics in HESEL is parametrized. Transport of plasma across the

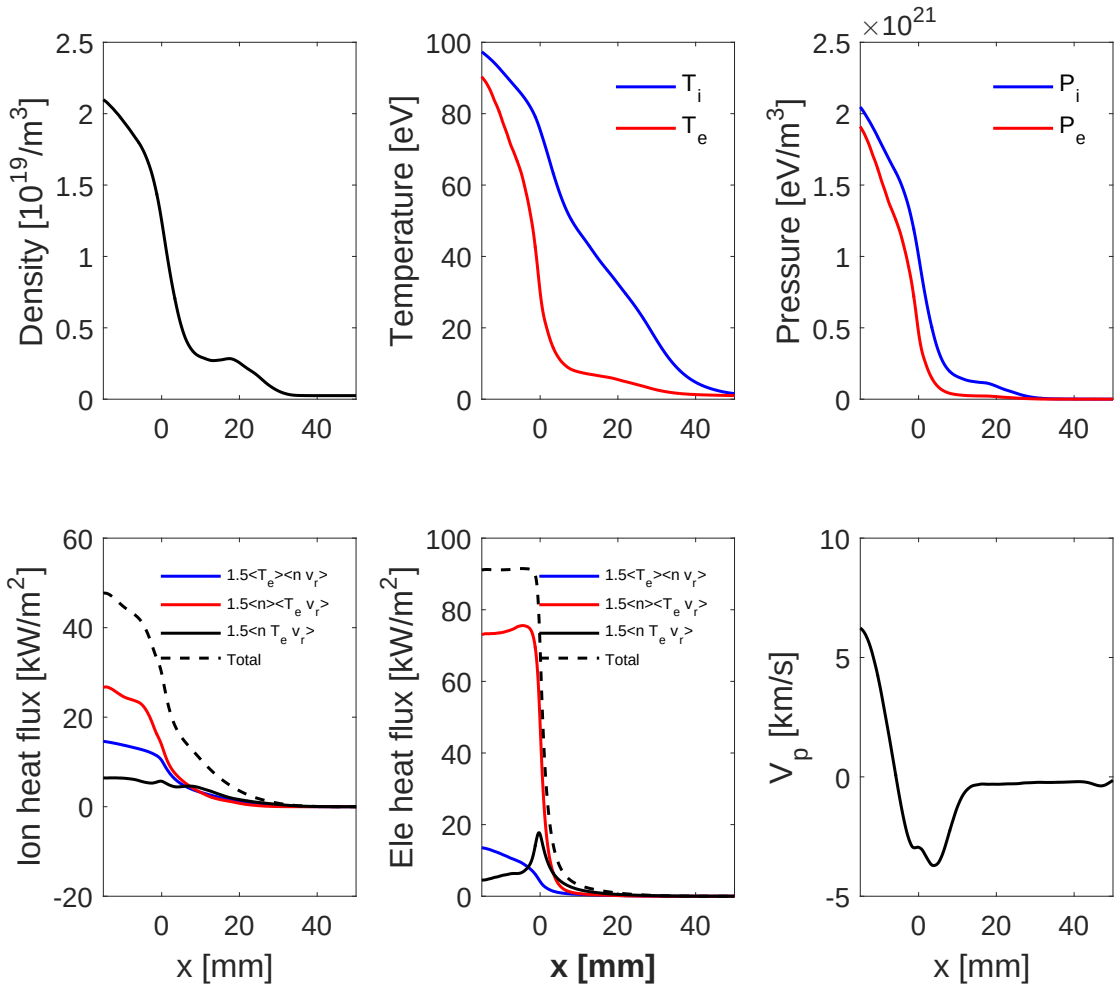

Figure 9: Radial profiles of density, temperatures, pressures, turbulent energy fluxes divided into convecting, conducting, triple product and total flux, and poloidal velocity. Data takes from the HESEL simulation presented in Fig. 2.

LCFS is concentrated in a region of 60 degree on the outboard midplane and we have used this fact to define a flux tube with a parallel ballooning length of $L_b = qR$. This length is used to parametrised parallel loses due to advection along the magnetic field lines. We are aware that parallel electron heat conduction is a relative fast process, and an equilibrium state stretching from the outboard midplane to the outer divertor establishes quickly, see e.g. [31]. We have in our model used the shorter parallel ballooning length for the electron heat conduction to include the fast decay of electron pressure in the SOL.

We have implemented the sheath condition in the model - linking the electron potential to the electron temperature in the SOL. This adds a significant sink for the poloidal velocity in the SOL. The sheath term is used to model connected and disconnected divertor conditions. In the connected condition we assume that both the mean and fluctuation part of the potential and electron temperature are coupled by

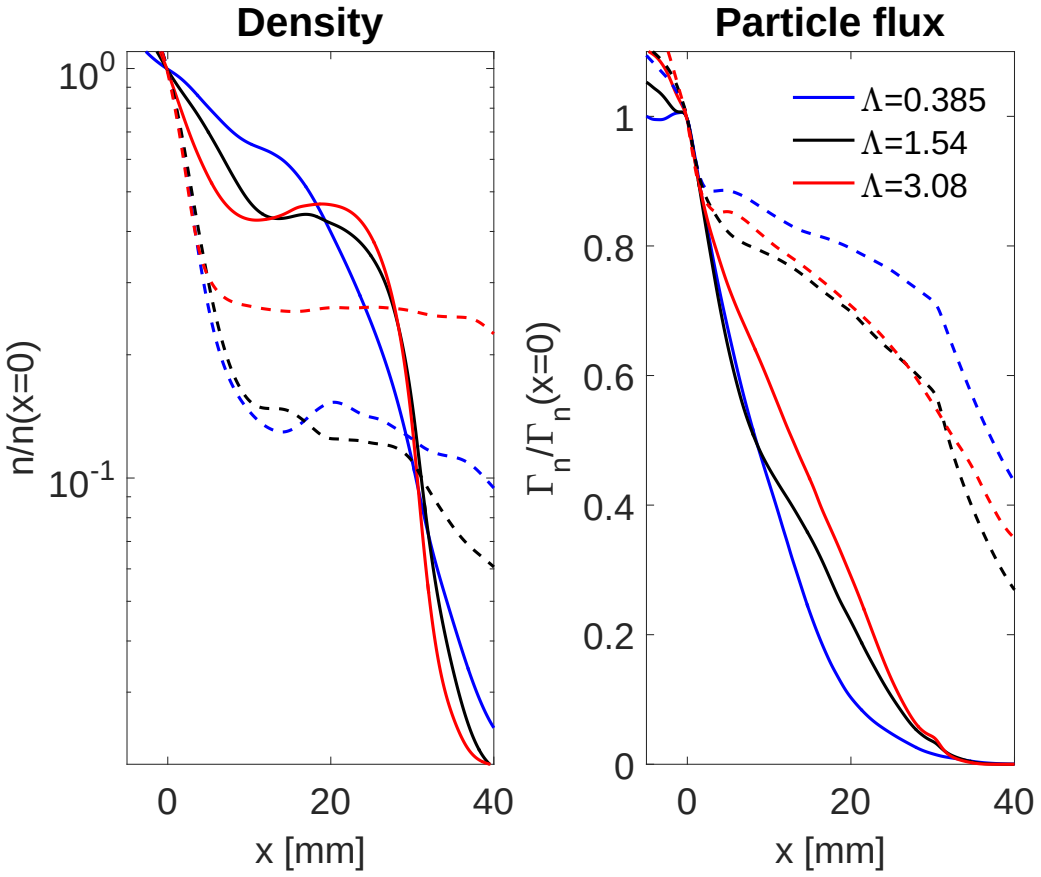

Figure 10: Radial profiles of density and turbulent perpendicular particle flux, $\Gamma_\perp$, in the SOL for different values of three connection lengths, L_c and thus of Λ. Full lines correspond to connected divertor condition and dashed lines to disconnected divertor condition. Input parameters as for Fig. 2 except $T_{e0} = T_{i0} = 20\,\mathrm{eV}$ and $L_{SOL} = 31\,\mathrm{mm}$.

the divertor sheath. Blobs being ejected into the SOL will in this case quickly loose momentum and will be left somewhere in the middle of the SOL to decay due to parallel loses. In the disconnected divertor conditions only the mean part of the potential and electron temperature are coupled by the divertor sheath. Strong and fast blobs would be generated and they will be able to cross the SOL and enter the wall region, interacting with the first wall in a toroidal device. If the connection length becomes too long we also would assume that the fluctuating part of the potential and electron temperature cannot coupled. Such a condition would be resemble a disconnected sheath condition in our model.

The inclusion of drift waves in the edge region has shown quite important for the observed instabilities in this region. Generally, we do not observed pure drift waves with a phase relation between density and radial velocity close to $\pi/2$ in this region, but the drift wave term controls the length scale of the instability which essentially will determine the size of the blobs being ejected into the SOL. This model is thus not significantly affected by the choice of aspect ratio of the numerical domain. The drift

wave terms are very sensitive to the choice of parallel length scale, as $\alpha \sim L_{\parallel}^{-2}$. The parallel length scales are in this paper chosen to to be equal the parallel ballooning length on open field lines, e.g. $L_b = L_{\parallel} = qR$. We observed blobs in the SOL with diameters of $1 - 2\,\mathrm{cm}$, in agreement with experimental observations, see e.g. [20]. A longer parallel length would result in larger blobs and for a length scale $L_{\parallel} < qR/4$ the gradients in the edge region would appear to be stable.

By varying the connection length, we are by simple means able to change the parameter Λ, the ratio between perpendicular to parallel transport, while keeping all other parameters constant in the model. The observed 'shoulder' formation in the density profile for increasing connection length is a result of local processes on the outboard midplane. We are, of course, aware that our parallel physics are simple, but we do notice that our results are in qualitative agreement with experimental observations in COMPASS, AUG and JET, see [18, 19] as well as in agreement with an older comparison between the numerical model, ESEL and Langmuir probe measurements at TCV, see [32, 33].

Finally, we have demonstrated that the energy transport across the SOL, and thus also the energy transport to the divertor region is strongly intermittent and the non-linear triple products in the energy flux terms are dominant. Energy transport is dominated by blob dynamics and we can observe a significant energy transport far into the SOL even in the case of flat density and temperature profiles.

5. Acknowledgements

This work has been carried out within the framework of the EUROfusion Consortium and has received funding from the Euratom research and training programme 20142018 under grant agreement No. 633053. The views and opinions expressed herein do not necessarily reflect those of the European Commission.This work was supported by the National Magnetic Confinement Fusion Science Program of China under Contracts No. 2015GB101000, by National Natural Science Foundation of China under Contracts No. 11422546 and 11575235 and the Sino-Danish Center for Education and Research (SDC).

References

[1] Nielsen A H, Xu G S, Madsen J, Naulin V, Juul Rasmussen J and Wan B N 2015 *Physics Letters. Section A: General, Atomic and Solid State Physics* **379** 3097–3101 ISSN 0375-9601

[2] Juul Rasmussen J, Nielsen A H, Madsen J, Naulin V and Xu G S 2015 *Plasma Physics and Controlled Fusion* **58** 014031 ISSN 0741-3335

[3] Olsen J, Madsen J, Nielsen A H, Rasmussen J J and Naulin V 2016 *Plasma Physics and Controlled Fusion* **58** 044011 URL `http://stacks.iop.org/0741-3335/58/i=4/a=044011`

[4] Madsen J, Naulin V, Nielsen A H and Rasmussen J J 2016 *Physics of Plasmas* **23** 032306 ISSN 10897674, 1070664x

[5] Braginskii S 1965 *In Review of Plasma Physics, (ed. Leontovich, M. A.). New York, NY: Consultants Bureau* **Vol. 1** 205–311

[6] Fundamenski W, Garcia O E, Naulin V, Pitts R A, Nielsen A H, Juul Rasmussen J, Horacek J, Graves J P and contributors J E 2007 *Nuclear Fusion* **47** 417–433 ISSN 00295515, 17414326

[7] Militello F, Tamain P, Fundamenski W, Kirk A, Naulin V and Nielsen A H 2013 *Plasma Physics and Controlled Fusion* **55** 025005 ISSN 07413335, 13616587

[8] Yan N, Nielsen A H, Xu G, Naulin V, Juul Rasmussen J, Madsen J, Wang H Q, Liu S C, Zhang W, Wang L and Wan B N 2013 *Plasma Physics and Controlled Fusion* **55** 115007 ISSN 07413335, 13616587

[9] Garcia O E, Nielsen A H, Naulin V and Juul Rasmussen J 2006 *Plasma Physics and Controlled Fusion* **48** L1–L10 ISSN 07413335, 13616587

[10] Xu G, Shao L, Liu S, Wang H, Wan B, Guo H, Diamond P, Tynan G, Xu M, Zweben S, Naulin V, Nielsen A H, Juul Rasmussen J, Fedorczak N, Manz P, Miki K, Yan N, Chen R, Cao B, Chen L, Wang L, Zhang W and Gong X 2014 *Nuclear Fusion* **54** 013007 ISSN 00295515, 17414326

[11] Ryter F, Orte L B, Kurzan B, McDermott R M, Tardini G, Viezzer E, Bernert M and Fischer R 2014 *Nuclear Fusion* **54** 083003 ISSN 00295515, 17414326

[12] Wu X, Xu G, Wan B, Juul Rasmussen J, Naulin V and Nielsen A H 2015 *NUCLEAR FUSION* **55** ISSN 00295515, 17414326

[13] Adamek J, Horacek J, Mueller H W, Rohde V, Ionita C, Schrittwieser R, Mehlmann F, Kurzan B, Stoeckel J, Dejarnac R, Weinzettl V, Seidl J, Peterka M and Team A U 2010 *Contributions To Plasma Physics* **50** 854–859 ISSN 15213986, 08631042

[14] Allan S Y, Elmore S, Fishpool G, Dudson B, Team M and Team E M 2016 *Plasma Physics and Controlled Fusion* **58** 045014 ISSN 13616587, 07413335

[15] Kocan M, Gennrich F P, Kendl A, Mueller H W and Team A U 2012 *Plasma Physics and Controlled Fusion* **54** 085009 ISSN 13616587, 07413335

[16] Myra J R, Russell D A and D'Ippolito D A 2006 *Physics of Plasmas* **13** 112502–1–9 ISSN 1070664x, 10897674

[17] Garcia O E, Horacek J, Pitts R, Nielsen A H, Fundamenski W, Naulin V and Juul Rasmussen J 2007 *Nuclear Fusion* **47** 667–676 ISSN 10185577, 00295515, 17414326

[18] Carralero D, Birkenmeier G, Muller H W, Manz P, deMarne P, Muller S H, Reimold F, Stroth U, Wischmeier M and Wolfrum E 2014 *Nuclear Fusion* **54** 123005 ISSN 00295515, 17414326

[19] Carralero D, Mueller H W, Groth M, Komm M, Adamek J, Birkenmeier G, Brix M, Janky F, Hacek P, Marsen S, Reimold F, Silva C, Stroth U, Wischmeier M, Wolfrum E, Team A U, Team C and Contributors J E 2015 *Journal of Nuclear Materials* **463** 123–127 ISSN 18734820, 00223115

[20] Zweben S J, Myra J R, Davis W M, D'Ippolito D A, Gray T K, Kaye S M, LeBlanc B P, Maqueda R J, Russell D A, Stotler D P and Team N U 2016 *Plasma Physics and Controlled Fusion* **58** 044007 ISSN 13616587, 07413335

[21] Johnsen H, Pecseli H L and Trulsen J 1987 *Physics of Fluids* **30** 2239–2254 ISSN 00319171, 21634998

[22] Naulin V and Nielsen A 2003 *Siam Journal on Scientific Computing* **25** 104–126 ISSN 10957197, 10648275

[23] Gunn J, Boucher C and Dionne M 2007 *Journal of Nuclear Materials* **363-365** 484 ISSN 00223115, 18734820

[24] Myra J R, D'Ippolito D A and Russell D A 2015 *Physics of Plasmas* **22** 042516 ISSN 1070664x, 10897674

[25] Myra J R, Russell D A and DIppolito D A 2008 *Physics of Plasmas* **15** 032304–1–13 ISSN 1070664x, 10897674

[26] Huld T, Iizuka S, Pecseli H and Juul Rasmussen J 1988 *Plasma Physics and Controlled Fusion* **30** 1297–1318 ISSN 13616587, 07413335

[27] Huld T, Nielsen A, Pecseli H and Juul Rasmussen J 1991 *Physics of Fluids B-plasma Physics* **3** 1609–1625 ISSN 2163503x, 08998221

[28] Nielsen A, Pecseli H and Juul Rasmussen J 1996 *Physics of Plasmas* **3** 1530–1544 ISSN 10897674,

1070664x

[29] GUZDAR P, DRAKE J, MCCARTHY D, HASSAM A and LIU C 1993 *Physics of Fluids B-plasma Physics* **5** 3712–3727 ISSN 2163503x, 08998221

[30] Scott B 2005 *Physics of Plasmas* **12** 1–23 ISSN 10897674, 1070664x

[31] Havlickova E, Fundamenski W, Tskhakaya D, Manfredi G and Moulton D 2012 *Plasma Physics and Controlled Fusion* **54** 045002 ISSN 13616587, 07413335

[32] Garcia O E, Pitts R A, Horacek J, Nielsen A H, Fundamenski W, Graves J P, Naulin V and Juul Rasmussen J 2007 *Journal of Nuclear Materials* **363-365** 575–580 ISSN 00223115, 18734820

[33] Garcia O E, Pitts R, Horacek J, Madsen J, Naulin V, Nielsen A H and Juul Rasmussen J 2007 *Plasma Physics and Controlled Fusion* **49** B47–B57 ISSN 13616587, 07413335